Remote Sensing of Environment 259 (2021) 112433

Contents lists available at ScienceDirect

Remote Sensing of Environment

journal homepage: www.elsevier.com/locate/rse

# Impact of the reproductive organs on crop BRDF as observed from a UAV

Wenjuan Li [a,b,1,*], Jingyi Jiang [a,d,1], Marie Weiss [a], Simon Madec [a], Franck Tison [a], Burger Philippe [c], Alexis Comar [b], Frédéric Baret [a]

[a] INRAE, Avignon Université, UMR EMMAH, F-84000 Avignon, France
[b] HIPHEN, F-84000 Avignon, France
[c] INRAE, UMR AGIR, Toulouse, France
[d] Research Center of Forest Management Engineering of State Forestry and Grassland Administration, Beijing Forestry University, 100083 Beijing, China

ARTICLE INFO

Editor: Jing M. Chen

*Keywords:*
BRDF
Wheat
Maize
Sunflower
Reproductive organs
UAV
Row effect

ABSTRACT

Several crops bear reproductive organs (RO) at the top of the canopy after the flowering stage, such as ears for wheat, tassels for maize, and heads for sunflowers. RO present specific architecture and optical properties as compared to leaves and stems, which may impact canopy reflectance. This study aims to understand and quantify the influence of RO on the bi-directional variation of canopy reflectance and NDVI.

Multispectral camera observations from a UAV were completed over wheat, maize, and sunflower just after flowering when the RO are fully developed and the leaf layer with only marginal senescence. The flights were designed to sample the BRDF with view zenith angles spanning from nadir to 60°and many compass directions. Three flights corresponding to three sun positions were completed under clear sly conditions. The camera was always pointing to two adjacent plots of few tenths of square meters: the RO were manually removed on one plot, while the other plot was kept undisturbed.

Results showed that the three visible bands (450 nm, 570 nm, 675 nm), and in a lesser way the red edge band (730 nm) were strongly correlated. We, therefore, focused on the 675 nm and 850 nm bands. The Bi-Directional Reflectance (BRF) of the canopy without RO shows that the BRF values were almost symmetrical across the principal plane, even for maize and sunflower canopies with a strong row structure. Examination of the BRF difference between the canopy with and without RO indicate that the RO impact canopy BRDF for the three crops. The magnitude of the impacts depends on crop, wavelength and observational geometry. These observations are generally consistent with realistic 3D reflectance simulations. However, some discrepancies were noticed, mainly explained by the small magnitude of the RO effect on canopy BRF, and the approximations made when simulating the RO layer and its coupling with the bottom canopy layer. We finally demonstrated that the RO layer impact the estimates of canopy traits such as GAI as derived from the multispectral observations.

## 1. Introduction

Continuous monitoring of crop growth is required for many applications including the evaluation of available resources, precision agriculture (McBRATNEY et al., 2005), and plant phenotyping (Comar et al., 2012). Remote sensing from satellites, planes, or UAVs (Unmanned Aerial Vehicles) are well-suited to describe the crop dynamics from reflectance acquired in several spectral bands. The interpretation of the data in terms of structural and biochemical properties is usually achieved using two main approaches: (1) an empirical approach, based on a set of experiments where both reflectance and canopy characteristics are concurrently measured; (2) a physically based approach using radiative transfer model simulations. For both approaches, assumptions on canopy structure are required to improve the accuracy of canopy characteristics estimates. In the case of the empirical approach, knowledge of the species observed and on the developmental stage may improve the retrieval performances. Similarly, in the case of the physically-based approach, knowledge on the expected range of canopy structure and associated optical properties of the elements may significantly improve the estimates.

Apart from the canopy structure differences between species, major differences are experienced along the growth cycle because of the

* Correspondig author at: HIPHEN, F-84000 Avignon, France
*E-mail addresses:* wli@hiphen-plant.com, wenjuan.li122@gmail.com (W. Li).
[1] These authors contributed equally.

https://doi.org/10.1016/j.rse.2021.112433
Received 9 September 2020; Received in revised form 17 February 2021; Accepted 1 April 2021

appearance of the reproductive organs (RO). RO have structural and optical properties very different from those of the leaves: they are generally thicker than leaves with lower contents in chlorophyll and sometimes elements with specific colors such as petals. These differences are expected to impact the radiative transfer in the canopy significantly since the RO are often located at the top of the canopy to ease pollen and seed dissemination either by the insects, birds, or by the wind. However, only a few studies document the impact of RO on canopy reflectance. Cossani and Reynolds (2012) reported that wheat ears intercept up to 40% of the incident radiation around the flowering stage. Li et al. (2015) show that removing the ear layer at the flowering stage reduces normalized difference vegetation index (NDVI) values by up to 7% in relative values. This explains why Weiss et al. (2001) included explicitly an ear layer to describe the wheat canopy structure and simulate crop reflectance along the growth cycle. Gitelson (2003) and Viña et al. (2004) showed that the presence of the tassels at the top of maize canopies induced a significant decrease of the VARI index. Wanjura and Hatfield (1988) investigated variations in canopy reflectance of sorghum, cotton, and sunflower crops during the growth cycle using the scattering and absorption coefficients. However, they were not able to draw clear conclusions on the impact of sorghum panicles and sunflower heads on canopy reflectance for the Landsat TM bands. More detailed investigations are thus required to better quantify the role of RO on canopy reflectance.

Canopy reflectance depends on the observational configuration. Therefore, the impact of RO on canopy reflectance should be investigated for the possible view and illumination directions under which crops are usually observed from various remote sensing platforms. Few studies report detailed measurements of the Bidirectional Reflectance Distribution Function (BRDF) (Nicodemus et al., 1977; Schaepman-Strub et al., 2006) for crops under field conditions. Goniometers have been used in the lab and in the field to characterize the BRDF (Sandmeier and Itten, 1999). However, their use is tedious and time-consuming, while generally corresponding to a very small footprint, questioning its suitability for characterizing the BRDF of tall crops such as maize and sunflower. Alternative airborne instruments such as the Parabola (Deering and Leone, 1986) and Airborne POLDER (Jacob et al., 2002) have been used to measure the BRDF of a range of canopies. They require specific flight design to sample the BRDF over a given target. The recent development of UAVs allows now to easily document the surface BRDF. Different sampling schemes have been used depending on the camera field of view. For a camera equipped with a wide field of view, the UAV is either moving along different tracks to sample the same target from several positions and directions (Hakala et al., 2013) or tilting the camera from about half the total field of view and keeping the UAV at about the same position while rotating in the compass direction (Roosjen et al., 2016). This later technique assumes that the surface is sufficiently homogenous to build the BRDF from points located at different places in the scene. For the small field of view cameras, the UAV is moving around the target while the orientation in view zenith and azimuth is changed continuously to keep the camera pointing towards the target (Burkart et al., 2015; Burkart et al., 2014; Grenzdörffer and Niemeyer, 2012). UAVs appear thus very convenient to document the surface BRDF.

Crop 3D modeling offers an efficient way to generate realistic canopies and simulate the associated reflectance for a range of source and view directions (España et al., 1999). Several open-source 3D ray tracing render engines were developed concurrently for computer graphics applications, such as LuxCoreRender (LuxCoreRender, 2018), MITSUBA (Jacob, 2014), and Pov-ray (POV-team, 2013). They have been successfully used by the remote sensing community to simulate canopy reflectance for a range of vegetation types (Casa and Jones, 2005; Disney et al., 2006; Duthoit et al., 2008; España et al., 1999; Génard et al., 2000; Jiang et al., 2020; Lopez-Lozano et al., 2009). However, most studies focus on crops before the reproductive stage: very few authors have included RO in their simulations due to the complexity of their morphology, topology, and optical properties.

The objective of this study is to quantify the influence of the RO on canopy BRDF in the visible and near-infrared (NIR) spectral domains. We present a new experimental design to measure canopy BRDF using a multispectral camera onboard an UAV. This allowed evaluating the influence of reproductive organs on the spectral and directional behavior of canopy reflectance. Three main crops are studied, with very different RO at the top of the canopy layer: wheat, maize, and sunflower. Field experiments were conducted for the three species during the reproductive stage to compare the BRDF measured from a UAV between the canopy with and without the RO. These measurements are complemented by reflectance simulations over 3D virtual scenes to better understand and quantify the impact of RO.

## 2. Materials and methods

### 2.1. Experimental sites and crops sampled

The wheat, maize, and sunflower experiments were located in Avignon, France (43.9°N, 4.9°E). The study focused on fully developed crops soon after the flowering stage, when the final height was reached and all leaves were fully developed with only a little senescence appearing at the bottom of the canopy. The wheat (*ISILDUR*) ears were mostly green and bearing awns, the tassels of maize (*Zea mays*) were light yellow. The heads of the sunflower (*MAS 88 OL*) were bearing yellow petals, the flower heads mostly facing the soil. Its back was green, and well seen from the top of the canopy. Note that the rows were oriented East-West for the three experiments (Table 1).

The sites were selected in a 20 × 20 m homogeneous area of the field. Two micro plots of at least 5 × 5 $m^2$ area were considered, one with the RO manually removed (RO-), the other (RO+) being undisturbed (Fig. 1). A 0.6 × 0.6 $m^2$ reference panel was placed horizontally slightly higher than the surrounding canopy to avoid possible interactions with the crops and between the two micro plots (Fig. 1). Four circular gray panels of 60 cm diameter were additionally placed on the four corners of the 20 × 20 $m^2$ site (Fig. 1) to be used as ground control points (GCP) for accurate projection of the images taken from the UAV. The coordinates of the center of the two reference panels and the four GCPs were measured with an RTK GPS (Trimble Geo 7 ×, 2 cm precision).

### 2.2. UAV experiment for BRDF characterization

A hexacopter UAV designed by Atechsys (http://atechsys.fr/) was carrying the AIRPHEN multispectral camera (https://www.hiphen-plant.com/our-solutions/airphen/). The camera had 6 spectral bands with 10 nm full width at half maximum. Five bands were equipped with an 8 mm focal length (450 nm, 530 nm, 675 nm, 730 nm, and 850 nm), which provided a field of view (FOV) of 33° × 25°. The sixth band (570 nm) was equipped with a 4.2 mm focal length providing a 60° × 46°

**Table 1**
Summary of the flights over wheat, maize, and sunflower experiments. The row azimuth, measurement date, take-off time, average sun zenith ($\theta_s$) and azimuth ($\varphi_s$) and illumination conditions during the flight are indicated. The azimuth angles are calculated regarding the North.

| Species | Date | Row azimuth (°) | Time (GMT + 1) | $\theta_s$ (°) | $\varphi_s$ (°) |
|---|---|---|---|---|---|
| Wheat | 23/05/2017 | 90.1 | 15:09 | 30 | 226 |
| | | | 16:12 | 40 | 246 |
| | | | 09:00 | 61 | 91 |
| Maize | 08/08/2016 | 89.2 | 14:17 | 29 | 221 |
| | | | 16:26 | 44 | 244 |
| | | | 18:00 | 61 | 264 |
| Sunflower | 28/07/2017 | 90.5 | 12:20 | 30 | 137 |
| | | | 10:40 | 45 | 108 |
| | | | 09:20 | 60 | 89 |

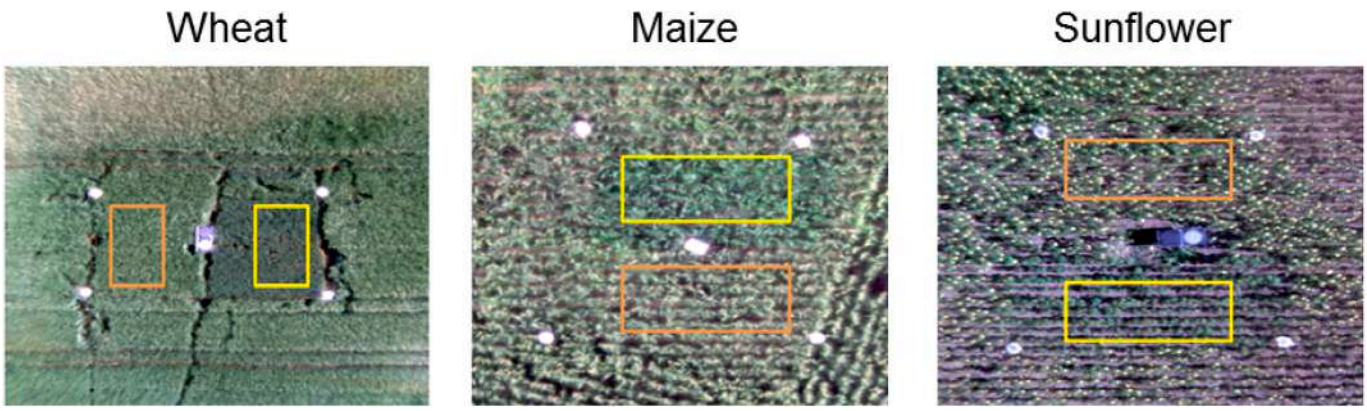


**Fig. 1.** The three experiments showing the RO+ (with RO, orange rectangle) and RO- (without RO, yellow rectangle) micro plots, the ground control points (GCPs), and the reference panel in the middle. (For interpretation of the references to colour in this figure legend, the reader is referred to the web version of this article.)

FOV. The 4.2 mm lens benefits from a higher overlap (80%) at the expense of a lower spatial resolution (4.06 cm at nadir). It was thus only used to improve the image alignment while the 8 mm lenses for the five other bands were used in the following of the study for their highest spatial resolution (2.11 cm at nadir). Besides the lower spatial resolution, the 4.2 mm lens at 570 nm would not add much spectral information as it is strongly correlated with the 8 mm lens at 530 nm. The camera was triggered every second, the integration time is automatically adjusted using a global shutter. The images were saved into a 12 bit TIFF format with metadata information including time of the acquisition, integration time, and GPS coordinates.

Over each site, the UAV flew three times during the day corresponding approximately to 30°, 45°, and 60° nominal sun zenith angles ($\theta_s$) (Table 1). For each $\theta_s$, the UAV sampled five view zenith angles ($\theta_v$ = [0°, 15°, 30°, 45°, 60°) for all view azimuth angles ($\varphi_v$) by flying along with five concentric circles, each one being at a specific altitude (Fig. 2). Two additional view zenith angles, $\theta_v = \theta_s$+5° and $\theta_v = \theta_s$-5° were complementing the five nominal $\theta_v$ angles to better sample directions close to the hotspot. The flight path was designed before the experiment and included an automatic adjustment of the compass orientation of the camera on the gimbal so that it was always pointing the reference gray panels, the view zenith angle being adjusted for each of the seven circles (Fig. 2). The distance to the ground along the view direction was around 45 m at maximum when cameras were close to the nadir direction (Fig. 2). This provided a ground spatial resolution of about 2.11 cm and 4.06 cm respectively for the 8 mm and 4.2 mm focal length. The UAV was flying at about 1 m/s speed and it took 7 to 10 min to sample all the view directions considered. During the UAV flights, the sky was clear without clouds (Table 1). The wind was gentle for maize and sunflower while significant for wheat with consequences on the faithful realization of the flight plan, with however no severe degradation of the sampling scheme.

### 2.3. Image extraction

The raw single frames taken concurrently by the six cameras were firstly co-registered to the reference image at 530 nm using the code developed by Rabatel and Labbé (2015). Vignetting effects were then corrected following the procedure proposed by Verger et al. (2014). Agisoft Photoscan software (Version 1.2.4.2399, Agisoft LLC., Russia) was then run using as input the images taken with the 530 nm and 570 nm cameras equipped respectively with 8 mm and 4.2 mm focal lengths. Agisoft Photoscan computed the corresponding position and orientation of the camera for each image. The GCPs were manually identified on the images and used to improve the georeferencing accuracy. The band at 570 nm was not used afterward because of the degraded resolution provided by the 4.2 mm focal length. Furthermore, it was mostly redundant with that at 530 nm with a higher spatial resolution. The pixels corresponding respectively to the two micro plots and the radiometric reference panel were then extracted for the five bands corresponding to the 8 mm focal lengths. The average digital number (DN) value was finally computed and associated with the corresponding integration time ($t$) and the view direction ($\theta_v$, $\varphi_v$). None of the images used were showing saturated pixels.

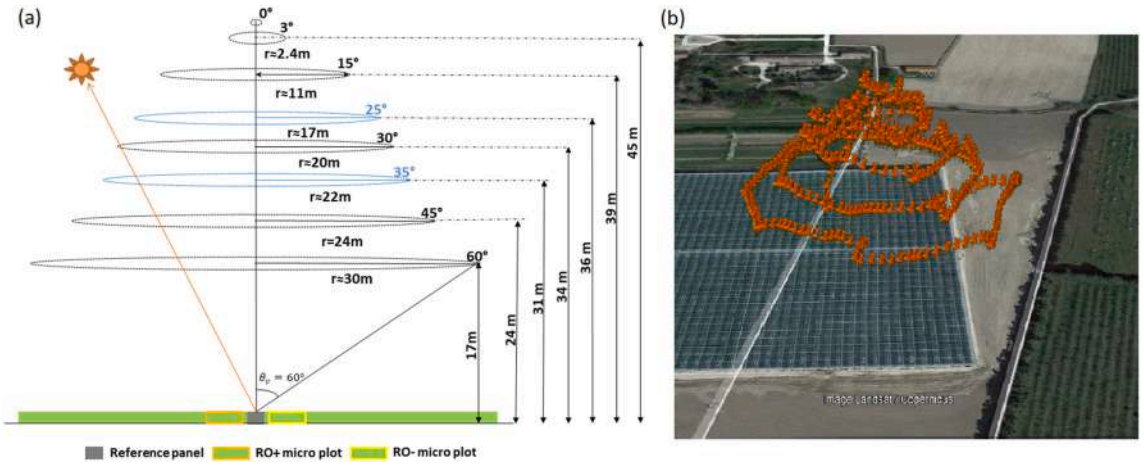


**Fig. 2.** (a) The flight plan for $\theta_s = 30°$; (b) the actual flight path over the maize experiment at 14:17 local time on 08/08/2016. RO+ and RO- represent micro plots with and without RO, respectively. The background image was from Google Earth™.

### 2.4. Radiometric calibration

The radiometric reference panel used in the field was made of a gray carpet that was previously characterized in the lab using a goniometer and a white spectralon as primary reflectance reference (Labsphere, Inc., North Sutton, NH, USA). Reflectance measurements were made with a spectral evolution SM-3500 spectrometer (www.spectralevolution.com). The Roujean BRDF model (Roujean et al., 1992) was then adjusted over the goniometer measurements. It was used to simulate the bi-directional reflectance (BRF) of the reference panel for any direction Ω. The 'gray' nature of the panel with all the bands having the same BRF value was well verified (Fig. 3). While the panel was relatively Lambertian for near nadir illumination, significant anisotropy is observed for $\theta_s > 30°$. For this reason, we preferred using only the nadir viewing observations for the radiometric calibration of the camera, assuming that the incoming radiation was stable during the flight.

The $BRF(\Omega, \lambda)$ of the canopy was computed from the DN values extracted from the images using the known BRF value of the reference panel ($BRF_{ref}$) and the DN values of the reference panel $DN_{ref}(\Omega, \lambda)$ extracted on the same image (Smith and Milton, 1999):

$$BRF(\Omega,\lambda) = \frac{DN(\Omega,\lambda)/t(\Omega,\lambda)}{DN_{ref}(\Omega o,\lambda)/t_{ref}(\Omega o,\lambda)} BRF_{ref}(\Omega o,\lambda) \quad (1)$$

where $\lambda$ is the wavelength, Ω corresponds to the observation configuration with $\Omega = [\theta_v, \varphi_v, \theta_s, \varphi_s]$ where $\theta$ and $\varphi$ represent respectively the zenith and azimuth angles, and subscripts v and s correspond respectively to the view and sun directions. $t$ is the integration time. The measurements of the reference panel used for the calibration correspond to viewing geometry close to the nadir direction noted here Ωo.

The radiance from the reference panel measured in the field includes a contribution of the direct sunlight as well as a diffuse component coming from the light scattered by the sky. The bi-directional reflectance measured in the lab was therefore converted into a blue-sky reflectance factor to account for the diffuse component. The hemispherical-directional reflectance factor was computed based on Roujean's model with the coefficients previously adjusted. The diffuse fraction was finally used to compute the corresponding blue-sky BRF (Schaepman-Strub et al., 2006). The diffuse fraction was derived from the 6S model simulations (Vermote et al., 1997) using the atmospheric characteristics measured from the local AERONET sun photometer as inputs (Holben et al., 1998).

Once the BRF at each measurement angle Ω was calculated, they were linearly interpolated from 0° to 60° zenith angles and from 0° to 360° azimuth angles with a 1° step for polar representation. Results are shown in the following analysis for the perpendicular and principal planes.

### 2.5. Reproductive organs characterization

For each crop, a sample of a representative RO was collected in the field. A set of photos were then taken with a SONY alpha 6000 RGB camera from multiple views: the organ was put vertically over a manually rotating plate in front of a uniform blue background. About 40 to 120 photos were taken by rotating the plate. These multi-view RGB photos were aligned using Agisoft Photoscan software (Version 1.2.4.2399, Agisoft LLC., Russia) to build a dense 3D point cloud used later to model the organ morphology. The lengths of wheat ears and maize tassels and the diameter of sunflower heads were also measured (Table 2). The optical properties in five bands were measured using the AIRPHEN camera: organs were placed horizontally over a black background and viewed from nadir under clear sky field conditions, the sun being at around 45° zenith angle. Organ surface reflectance was then computed using a reference panel placed horizontally in the camera field of view. Average values of sunlit wheat ears, maize tassels, and sunflower petals and front-side and back-side of the heads were then computed (Table 2, Table B1).

### 2.6. Reflectance simulations

The canopy was considered as composed of two layers, the top one corresponding to the RO. The bottom layer corresponds to the canopy without the RO. It was characterized by the measured BRF(Ω, $\lambda$) value over the RO- modality, with BRF value equal to that measured in the considered view-illumination geometry. The reproductive organ layer

**Table 2**
Fields and RO characteristics used for the 3D scene generation. The reflectance of sunflower frontside flower and backside flower does not include yellow petals.

| Characteristics | Unit | Wheat | Maize | Sunflower |
|---|---|---|---|---|
| RO- layer height (m) | m | 0.8 | 1.6 | 1.03 |
| RO- Green Area Index GAI[a] | – | 2.7 | 4.9 | 0.40 |
| Row spacing (m) | m | 0.155 | 0.77 | 0.63 |
| Density of RO (nb/m$^2$) | nb/m$^2$ | 450 | 8 | 4 |
| Length of RO (m) | m | 0.11 | 0.25 | |
| Diameter of RO (m)[b] | m | 0.015 | 0.005 | 0.25 |
| RO area index (m$^2$/m$^2$)[c] | – | 1.23 | 0.16 | 0.20 |
| Reflectance of RO @675 nm | – | 0.1 | 0.25 | Flower front-side: 0.122<br>Flower back-side: 0.25<br>Flower yellow petal: 0.34 |
| Reflectance of RO @850 nm | – | 0.45 | 0.7 | Flower front-side: 0.219<br>Flower back-side: 0.5<br>Flower yellow petal: 0.36 |

[a] GAI was estimated using a simple empirical model described in Verger et al. (2011) and based on the measured NDVI.
[b] Diameter of maize tassel corresponds to the mean value of all branches.
[c] RO area of wheat head is calculated as half the developed area of a cylinder. For maize, tassels were considered as made of five cylindric branches. The area of sunflower head was calculated as a disc.

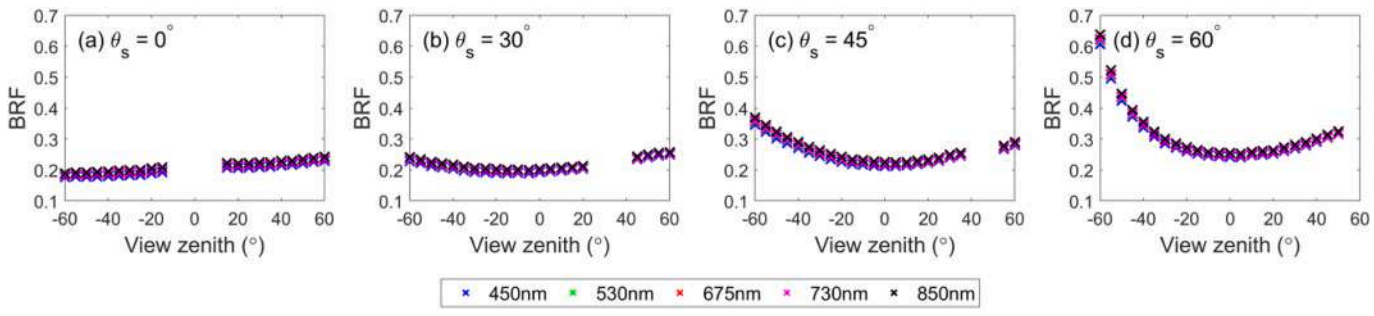


**Fig. 3.** BRF of the reference panel measured in the lab in the principal plane for four sun zenith angles as a function of the view zenith angle. Positive view zenith angles correspond to the backward direction, while negative values correspond to forward direction.

was built by replicating the typical reproductive organ (Table 2). For wheat, the ears were vertical and placed regularly according to the plant density For maize, the panicles were randomly oriented and placed according to the row spacing and plant density. For sunflowers, all the flowers were oriented towards the east and placed according to the row spacing and plant density. For the three crops, a small random shift of the nominal position was added to mimic the actual localization of the RO (Fig. 4). Scenes of 2.0 × 2.8 $m^2$ were built and replicated 179 times around the center one to avoid border effects. The reflectance of the RO material was assumed Lambertian and characterized by the corresponding measured reflectance (Table 2) with transmittance equal to zero.

Canopy reflectance with RO was simulated using the LuxCoreRender 3D render engine (LuxCoreRender, 2018). LuxCoreRender is open-source software (LuxCoreRender, 2018), which was validated with a set of state-of-the-art models by Jiang et al. (2020) using the RAMI Online Model Checker (ROMC) (Widlowski et al., 2008). We used the LuxCoreRender ray-tracing integrator with 128 rays per camera pixel to guarantee the accuracy of the simulated reflectance. A perspective camera was selected to simulate the AIRPHEN camera with a 33° x 25°field-of-view. For each $\theta_s = [30°, 45°, 60°]$, the observation configuration including $[\theta_v, \varphi_v]$ and the height of the camera was kept the same as in the field experiments. Since the three experiments were conducted under clear sky conditions, no diffuse sky light was considered in our simulations.

## 3. Results

### 3.1. Selecting a subset of bands for further analysis

The correlations between the red band (675 nm) and the other four bands were first analyzed to select a subset of bands that will be later investigated for the sake of clarity. Results (Table 3) show that the 450 nm and 530 nm bands were very strongly correlated to the 675 nm band for all sun zenith angles and the three experiments ($r^2 > 0.8$). This is explained by the marginal contribution of multiple scattering and the soil background as well as the fact that most of the elements have similar optical properties in the visible domain. Conversely, bands at 730 nm and mainly that at 850 nm show degraded correlations with the visible bands due mostly to the importance of the multiple scattering in the NIR domain. Therefore, we selected the 675 nm and 850 nm bands as a representative subset to illustrate in the following sections the impact of the RO on the directional reflectance.

### 3.2. Directional effects over the canopy without the reproductive organs (RO-)

Before quantifying the impact of the reproductive organs on canopy reflectance, the directional properties of the canopies without the RO (RO-) corresponding only to the leaf and stem layer over the soil background were first investigated. They will be used later to compute canopy BRDF using the simulated layer of RO.

#### 3.2.1. Main directional features

The directional features for the three crops and two bands show similar patterns across the three sun positions. We, therefore, illustrate it using only the measurements for $\theta_s = 45°$ (Fig. 5). Measurements for the other two sun directions are presented in Fig. A1 and Fig. A2. The polar plots were obtained by linear interpolation of the raw measured BRF in both zenith and azimuth directions with a 1° angular resolution. A peak corresponding to the sun direction is observed in the hotspot, i.e. when the shadows cast by the leaves or soil roughness are not seen (Qin and Goel, 1995). The hotspot is relatively narrow for the maize and sunflower crops both in the red and NIR bands, while it appears broader for te wheat in these two bands. Note that the hotspot is located in the South-Eastern compass directions for the sunflower experiments since measurements were completed in the morning (Table 1). Conversely, the hotspot is in the South-Western compass direction for maize and wheat, corresponding to afternoon flights. For directions opposite to the hotspot corresponding to the forward scattering, the reflectance is generally lower.

For the visible and NIR bands, the three crops show a general symmetry on both sides of the principal plane, i.e. the plane containing the sun direction (Fig. 5). To better evaluate the symmetry across the principal plane, for each 5° zenith by 5° azimuth cells, the BRF difference, $\delta BRF(\Omega, \lambda)$, with the average of the two symmetrical directions across the principal plane was computed: a perfectly symmetric BRDF with regards to the principal plane should verify $\delta BRF(\Omega, \lambda) = 0$. Results (Fig. 6) confirm that a general symmetry exists across the principal plane since the BRF differences of symmetrical directions are generally within $-0.01 < \delta BRF(\Omega, \lambda) < 0.01$. This is well verified for dense canopies such as maize for both bands (Fig. 6). This is also the case for wheat that presents little row structure at the flowering stage. Nevertheless, in the NIR, a slight dissymmetry is observed for the three sun directions, with slightly higher reflectance in the directions north to the principal plane (Fig. 6). The sunflower shows very similar patterns in both bands (Fig. 6). A persistent dissymmetry is observed for the three sun positions, with slightly higher reflectance in the directions south to the principal plane. Since the rows were oriented East-West, this can be easily explained for $\theta_s = 30°$ and $\theta_s = 45°$: the illuminated plants and soil in the row are preferentially seen from the southern directions as compared to the northern ones. This agrees very well with the results from (Ranson et al., 1985) as well as reflectance simulations of row canopies (Goel and Grier, 1987; Suits, 1983; Zhao et al., 2010). However, when the sun is almost parallel to the row direction as observed for $\theta_s = 60°$, the southern side appears more reflective than the northern one. This was not expected and is more difficult to explain unless invoking some non-isotropic distribution of leaf azimuthal directions, or some uncorrected

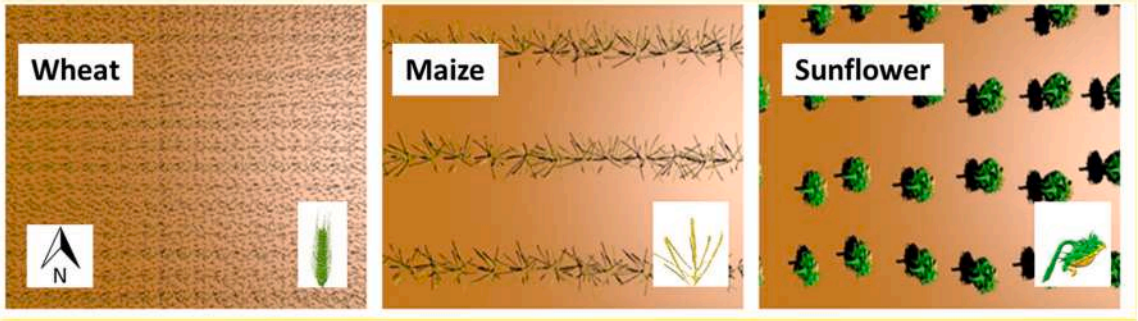


**Fig. 4.** Nadir view of the 3D scenes (2.0 × 2.8 $m^2$) for wheat, maize, and sunflower as rendered with Luxrender. The sun position is in the east at 45° zenith angle. The reproductive layer was put here on a brown background for better visualization. A side view of the typical reproductive organ replicated in the scene is also displayed for each crop. (For interpretation of the references to colour in this figure legend, the reader is referred to the web version of this article.)

**Table 3**
Correlation coefficients ($r^2$) between canopy reflectance @675 nm and the four other bands for wheat, maize, and sunflower experiments over all images. It includes RO- and RO+ observations for the three sun zenith angles ($\theta_s$).

| | $\theta_s$ | Wheat | | | | Maize | | | | Sunflower | | | |
|---|---|---|---|---|---|---|---|---|---|---|---|---|---|
| | (°) | 450 | 530 | 730 | 850 | 450 | 530 | 730 | 850 | 450 | 530 | 730 | 850 |
| RO+ | 30 | 0.95 | 0.95 | 0.9 | 0.75 | 0.99 | 0.98 | 0.89 | 0.65 | 0.96 | 0.95 | 0.72 | 0.63 |
| | 45 | 0.98 | 0.96 | 0.81 | 0.6 | 0.99 | 0.98 | 0.93 | 0.76 | 0.99 | 0.97 | 0.88 | 0.83 |
| | 60 | 1.00 | 1.00 | 0.98 | 0.96 | 0.99 | 0.98 | 0.93 | 0.8 | 0.99 | 0.97 | 0.91 | 0.86 |
| RO- | 30 | 0.81 | 0.91 | 0.8 | 0.44 | 0.99 | 0.97 | 0.91 | 0.66 | 0.94 | 0.93 | 0.8 | 0.73 |
| | 45 | 0.9 | 0.92 | 0.77 | 0.47 | 0.99 | 0.98 | 0.92 | 0.75 | 0.98 | 0.98 | 0.92 | 0.88 |
| | 60 | 0.97 | 0.98 | 0.93 | 0.84 | 0.99 | 0.96 | 0.89 | 0.68 | 0.98 | 0.98 | 0.94 | 0.89 |

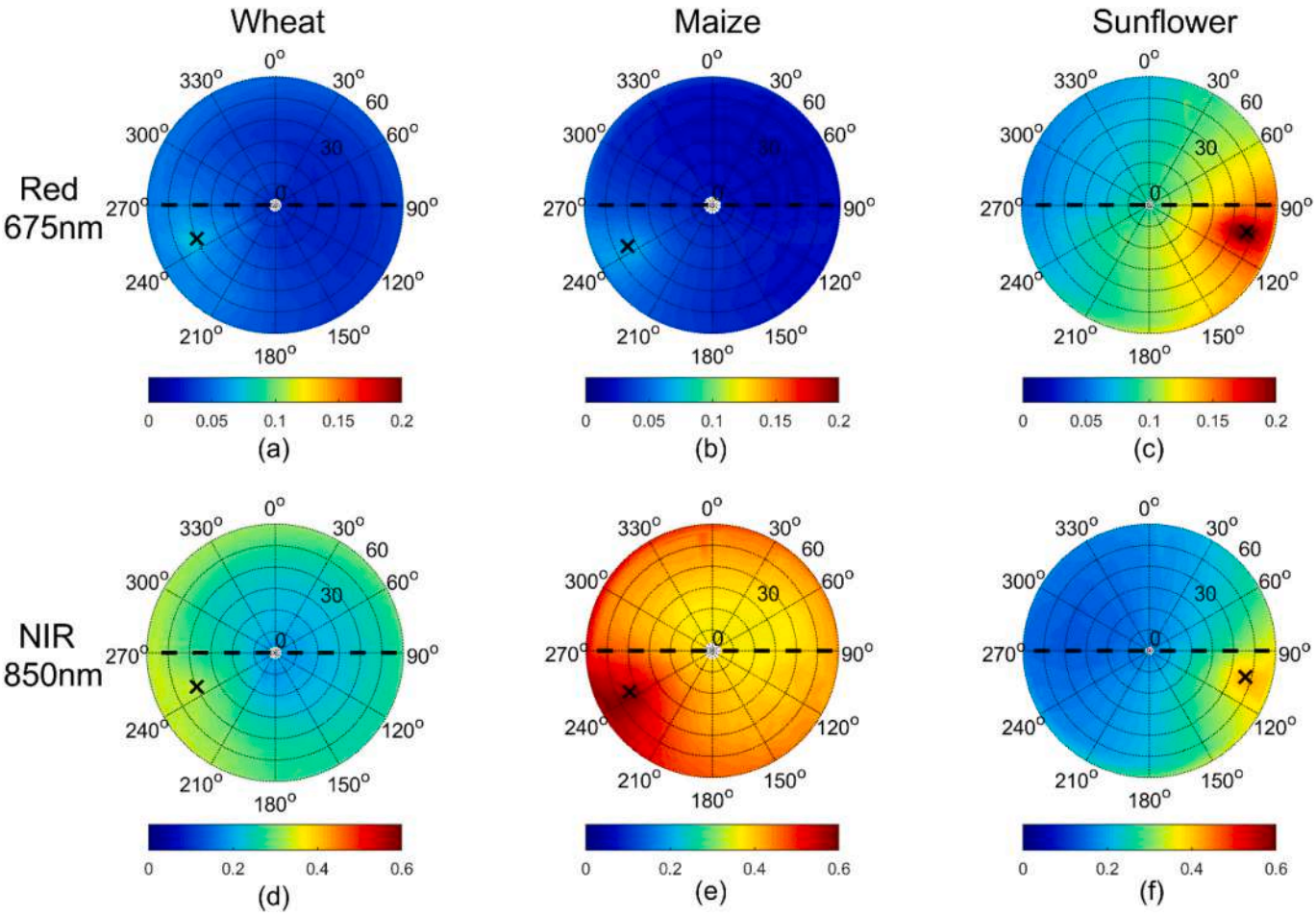


**Fig. 5.** Polar representation of the measured BRF distribution of the three experiments without the RO (RO-) for 675 nm and 850 nm bands. The sun is displayed as a black cross marker and was at $\theta_s$=45°. The row orientation (east-west) is represented by the dashed black line. Values represent interpolations from raw measured BRF.

biases in the measurements. However, the magnitude of the difference is generally lower than 0.01 which is probably close to the measurement uncertainties.

Because of the general symmetry across the principal plane, we will focus in the following on the average BRF between the two symmetrical directions across the principal plane. This will offer the advantage to

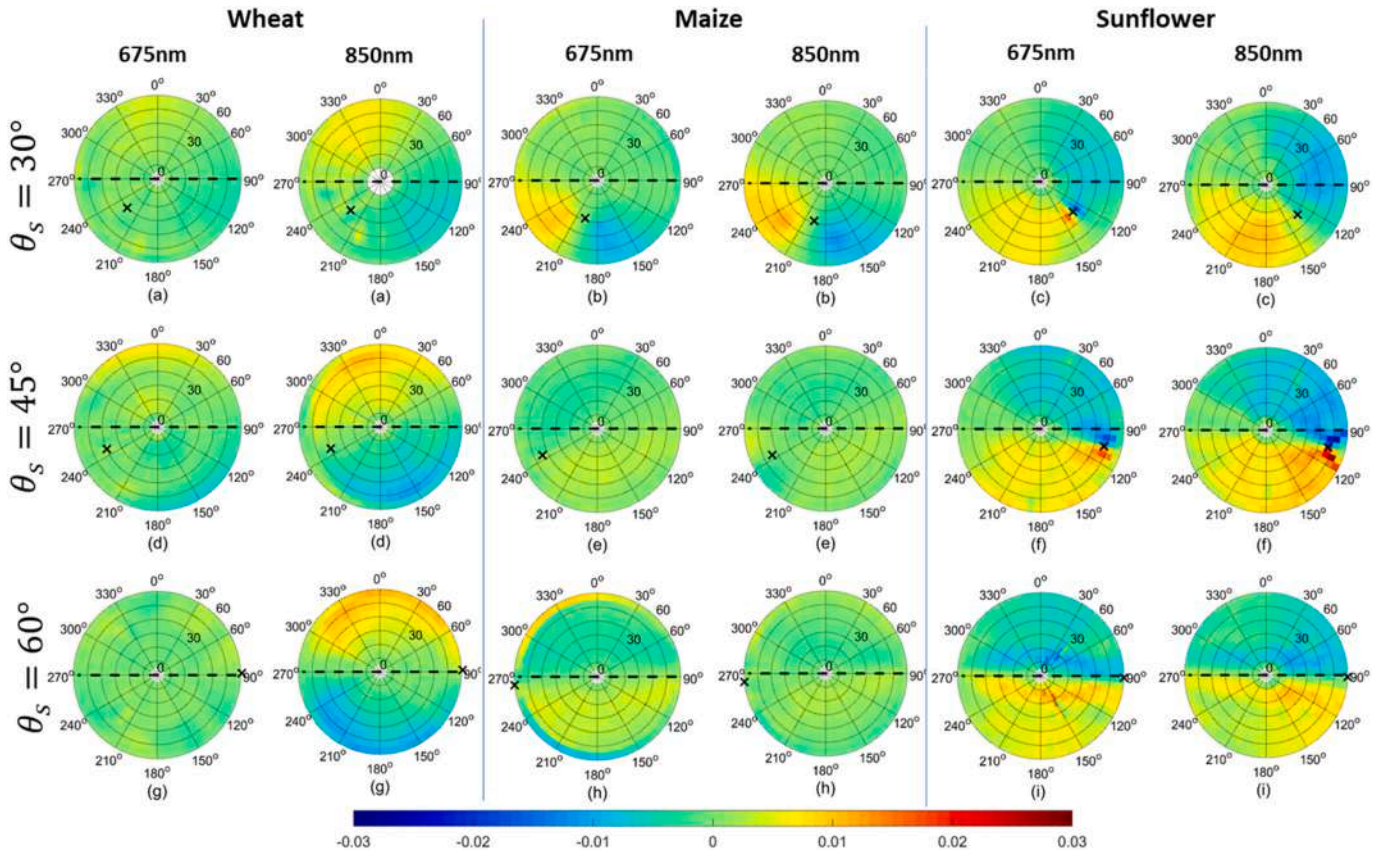


**Fig. 6.** Polar plot of $\delta BRF(\Omega, \lambda)$ for wheat, maize, and sunflower without RO @675 nm and 850 nm, and the three sun positions considered. $\delta BRF(\Omega, \lambda)$ represents for each view direction the BRF differences with the average BRF values of the two symmetrical directions across the principal plane: when $\delta BRF(\Omega, \lambda) = 0$, the BRF of both symmetrical directions across the principal planes are the same. The black cross marker represents the sun position during the flight. The black dashed line is the row direction.

smooth out possible local uncertainties.

### 3.2.2. *Directional effects in the principal plane*

The BRF in the principal plane was approximated as the BRF measured values within ±5° azimuth difference with that of the sun direction. All the crops, bands, and directions show similar patterns (Fig. 7) with however large differences in magnitude. The maximum BRF is observed always close to the hotspot direction as expected. The minimum BRF values are observed close to the nadir for the NIR band, and in the forward scattering directions for the visible bands. The difference between red and NIR bands depends on the species as a function of the green area index values: the wheat has the largest GAI and the largest difference between red and NIR. Conversely, sunflower has the lowest GAI and the lowest difference between the BRF in both domains.

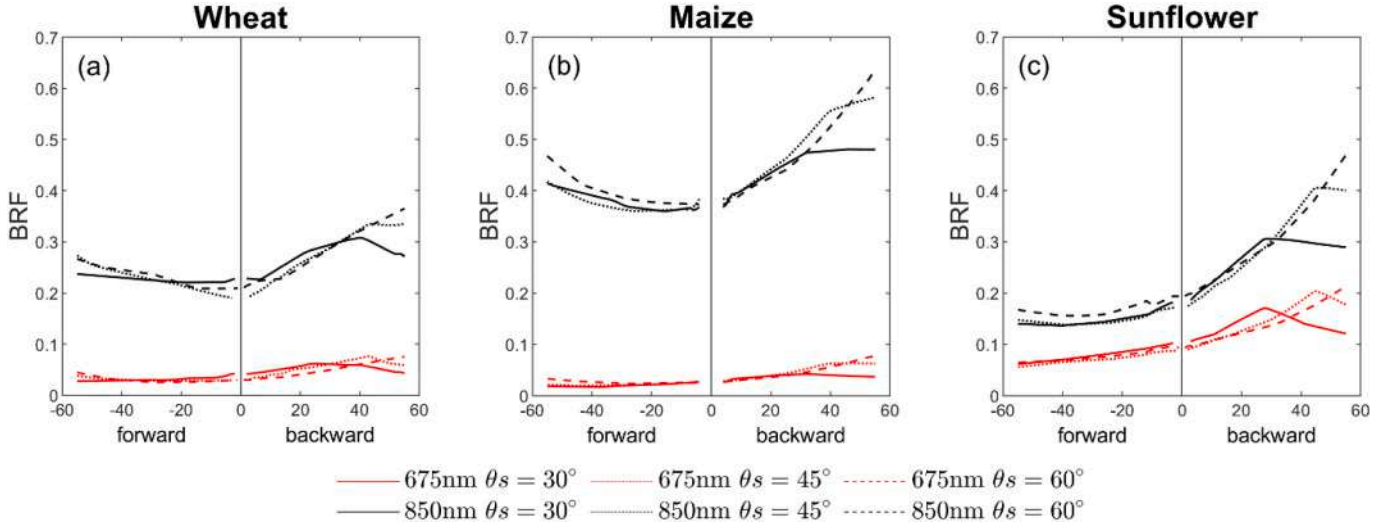


**Fig. 7.** BRF values in the red (675 nm) and NIR (850 nm) in the principal plane as a function of the view zenith angles. Observations over canopies without the RO for $\theta_s$=[30°, 45°, 60°]. (For interpretation of the references to colour in this figure legend, the reader is referred to the web version of this article.)

Outside the hotspot directions, small differences of BRFs are observed between the three sun directions with however slightly higher values for $\theta_s$= 60° for the more oblique view directions in the NIR, while the contrary is observed in the visible domain (Fig. 7).

### 3.3. Effects of reproductive organs on canopy reflectance

#### 3.3.1. Main directional features

We focused first on $\Delta BRF(\Omega,\lambda)$, i.e. the canopy BRF difference between canopy with organs (RO+) and without organs (RO-). This was computed based on the average BRF between the two symmetrical directions across the principal plane as explained earlier. Results show that the impact of RO on canopy BRF is relatively small in absolute value, with $-0.02 < \Delta BRF(\Omega,\lambda) < 0.02$ in the red, and $-0.04 < \Delta BRF(\Omega,\lambda) < 0.04$ in the NIR (Fig. 8). However, when computed in relative values, $\Delta BRF(\Omega,\lambda)$ can reach substantial levels up to 85% in the red because of the small $BRF(\Omega,\lambda)$ observed (Fig. 5) and up to 34% in the NIR. The impact of RO depends mainly on the crop, on the spectral domain as well as on the directions considered.

For wheat, the ears generally decrease canopy reflectance both in the red and NIR bands (Fig. 8). This is consistent with studies by Li et al. (2015). Little directional effects due to the sun and view directions are observed, with however larger impacts close to the hotspot. We observe some higher differences (in absolute value) for $\theta_v > 55°$, which may

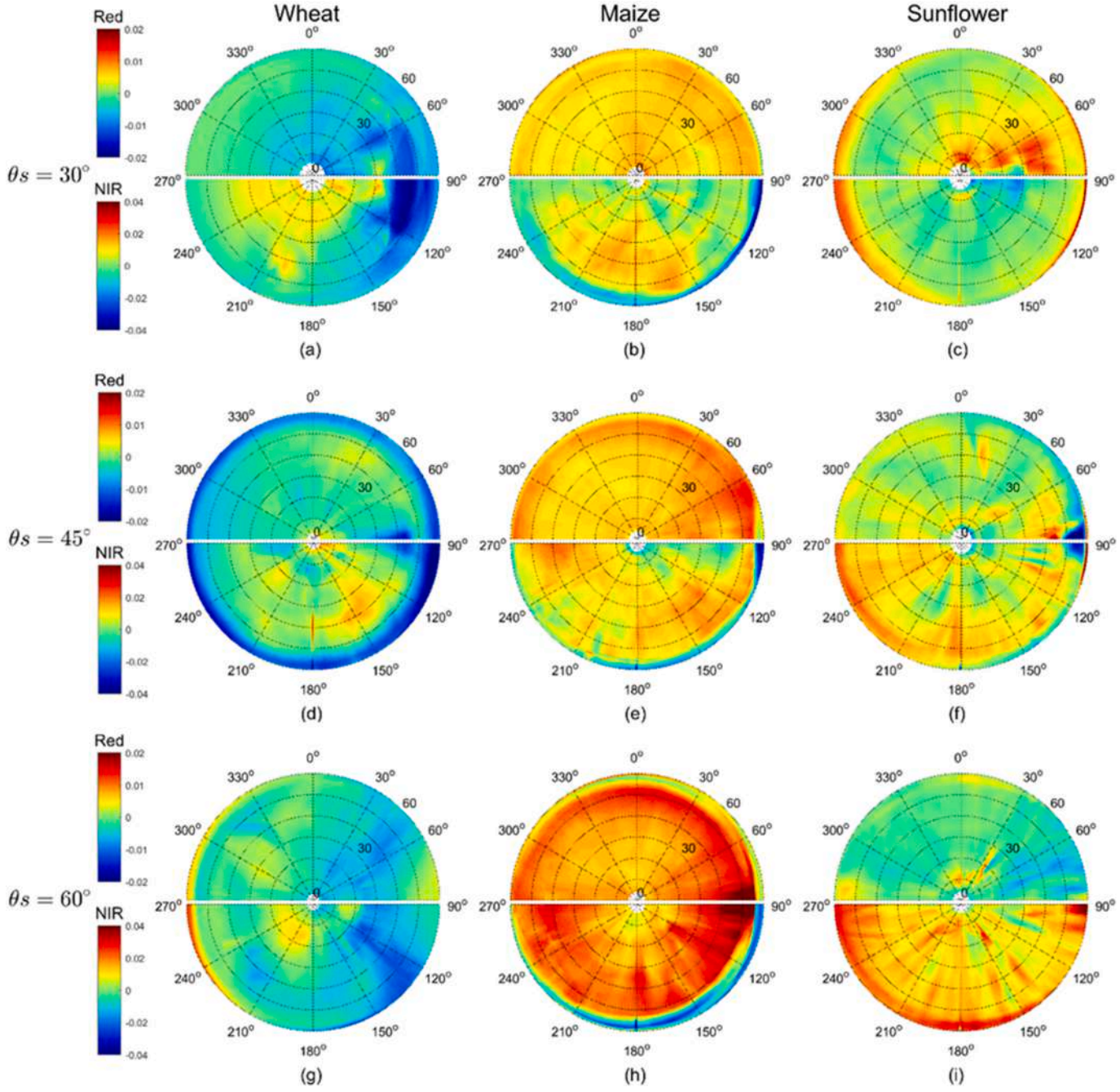


**Fig. 8.** Directional distribution of $\Delta BRF(\Omega,\lambda)$, the canopy BRF difference with (RO+) and without (RO-) the RO. Wheat (left), maize (middle), and sunflower (right) are displayed for $\theta_s$ = [30°,45°,60°]. Each half polar plot represents the average BRF values between the two symmetrical directions across the principal plane. The top hemisphere represents the red band and the bottom one the NIR band. The principal plane is in the 90° - 270° azimuthal direction, with the hotspot located on the right side (90° azimuth). (For interpretation of the references to colour in this figure legend, the reader is referred to the web version of this article.)

correspond to artifacts in the measurements. Similar artifacts are also noticed for maize and sunflower.

The tassels of maize generally increase canopy BRF for all sun and view directions both in the red and NIR domains. The impact increases substantially with the solar zenith angle, while the effect of view direction is marginal (Fig. 8).

For sunflower, the influence of heads is contrasted between the red and NIR domains: in the red, the impact is small with $\Delta BRF(\Omega,\lambda) \approx 0$ for the three sun directions; conversely, in the NIR, the heads increase canopy reflectance, particularly for the larger sun zenith angles (Fig. 8).

### 3.3.2. *Consistency between observations and simulations*

Since the experimental evidence of the impact of RO on canopy reflectance appears difficult due to the small differences observed and possible confounding measurement uncertainties, we wanted to consolidate the findings based on radiative transfer simulations. We concentrated on the principal plane where most directional features are expected and computed $\Delta BRF(\Omega,\lambda)$.

In the red domain (Fig. 9), simulations confirm that the impact of RO is small. It is slightly negative for wheat, slightly positive for maize, and neglectable for sunflower. For wheat, the addition of the ear layer representing an area index around 1.2 (Table 2) decreases canopy BRF since ears are green with low reflectance (Table 2) without transmitting light, i.e. a very absorbing layer. Furthermore, their vertical position acts as a light trap, increasing light absorption by the lower layers of the canopy. For maize, the tassels act as a scattering layer since they reflect more light than the lower layer of green vegetation due to their higher reflectance (Table 2). When the sun zenith increases, $\Delta BRF(\Omega,\lambda)$ increases because of the longer path length in the tassel layer. The same is also observed for more inclined views, particularly in the backward scattering direction. The small impact of sunflower heads on canopy reflectance can be explained by their small contribution in terms of area index (Table 2), on top of the green layer of leaves. The more subtle differences observed as a function of the observational geometry are difficult to explain.

In the NIR domain (Fig. 10), the small impact of the ears on $\Delta BRF(\Omega,\lambda)$ is explained by the light trap feature as described previously and the small scattering properties of the ears that do not transmit light. For maize, the discrepancies between measurements and simulations may be partly explained by the fact that the strong row structure of the vegetation layer was not accounted for in our simulations. Measurements show a positive impact of the tassels for $\theta_s = 60^\circ$ and oblique viewing. For the sunflower, the heads induce a slight increase of canopy reflectance, probably due to the high values of the reflectance of the back-side of heads (Table 2) that are pointing upward.

Furthermore, the discrepancies found between observed and simulated $\Delta BRF(\Omega,\lambda)$ values may be explained by the possible measurement uncertainties as well as the assumptions made for the canopy reflectance simulations regarding the spatial homogeneity (i.e. no row structure) of the bottom vegetation layer that is coupled with the RO layer.

## 3.4. *Impact on NDVI values and GAI estimation*

Previous results demonstrated that the effect of RO on canopy reflectance was variable in the visible and NIR bands. We thus investigated how NDVI (Rouse Jr. et al., 1973), a vegetation index widely used

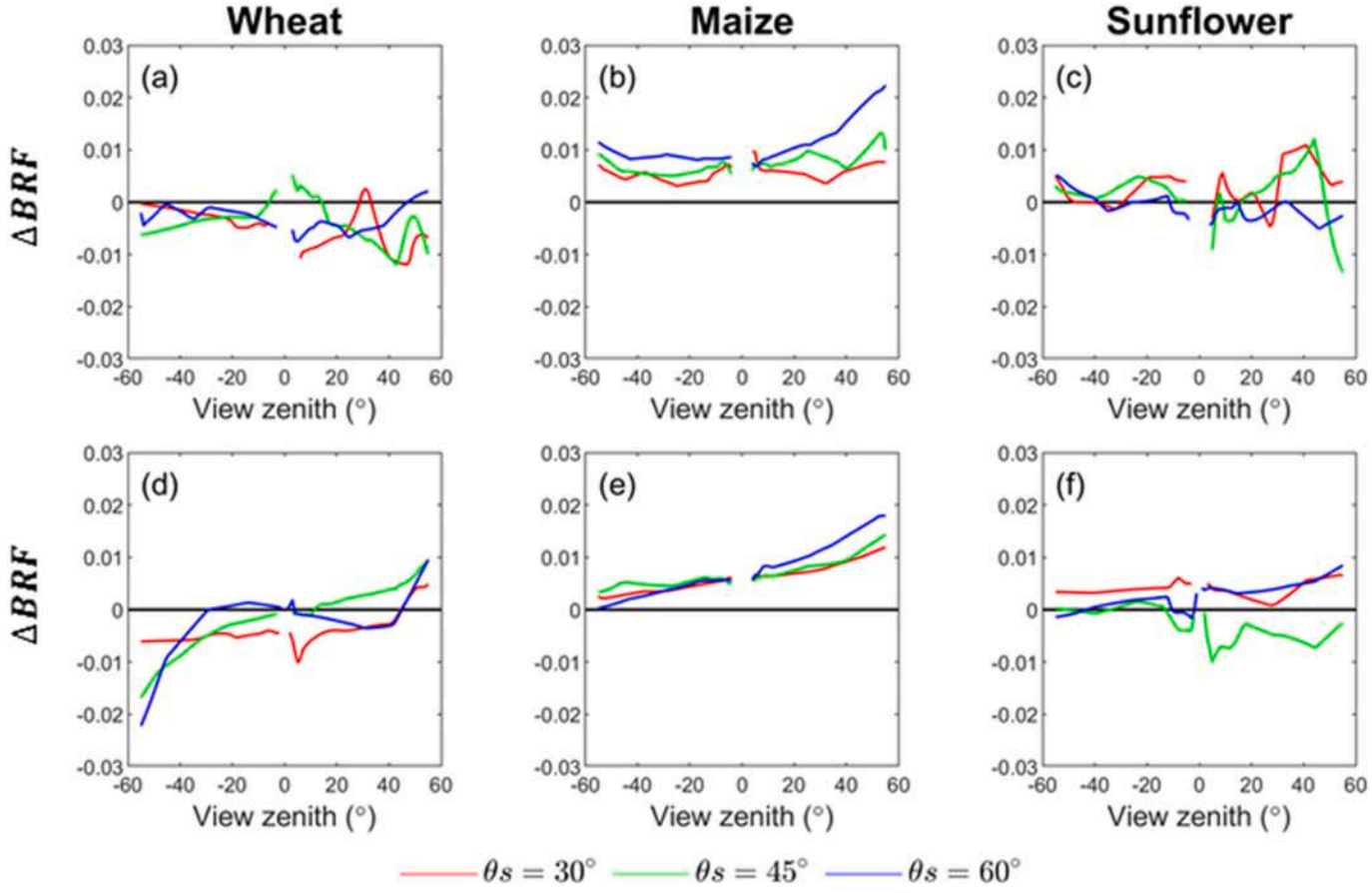


**Fig. 9.** Measured BRF differences between canopy with (RO+) and without (RO-) RO as a function of the view zenith angle in the principal plane at 675 nm from measurements (top) and 3D simulation (bottom). The back-scattering direction corresponds to positive view zenith angles. Crops are shown from left to right: wheat, maize, and sunflower. Several solar zenith angles are considered: $\theta_s = 30^\circ$ (red), $\theta_s = 45^\circ$ (green), and $\theta_s = 60^\circ$ (blue). (For interpretation of the references to colour in this figure legend, the reader is referred to the web version of this article.)

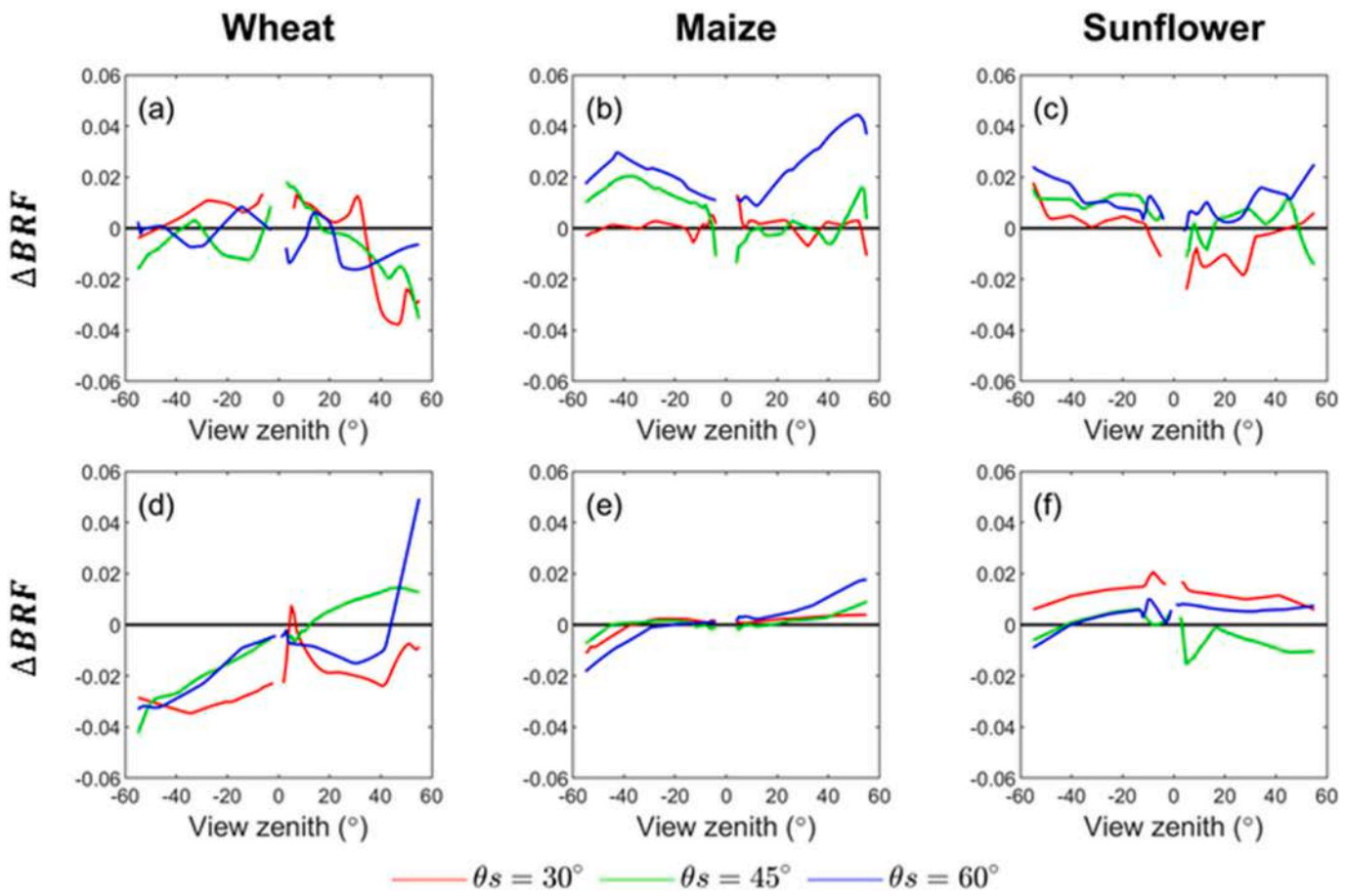


**Fig. 10.** Measured BRF differences between canopy with and without RO as a function of the view zenith angle in the principle plane at 850 nm from measurements (top) and 3D simulation (bottom). The back-scattering direction corresponds to positive view zenith angles. Crops are shown from left to right: wheat, maize, and sunflower (right) and different solar zenith angles are considered: $\theta_s$ of 30° (red), 45° (green) and 60° (blue). (For interpretation of the references to colour in this figure legend, the reader is referred to the web version of this article.)

to quantify vegetation amount and combining the red and NIR bands, was impacted by the RO. We focused here on near nadir observations ($-10^\circ < \theta_v < 10^\circ$), which is the typical geometry used to observe crops from high-spatial resolution satellites.

NDVI indicates the amount of green vegetation that can be also quantified by the green area index (GAI): a gradient is observed between wheat, maize, and sunflower as a function of the GAI value (Table 2), with maize having the larger GAI, and sunflower the lower one (Fig. 11). The addition of ears in wheat canopies increases the NDVI value. This is consistent with the results from Li et al. (2015) and is mainly explained by the green nature of the ears at the flowering stage that absorb strongly in the red and scatter light in the NIR. Note that the area index of the ear layer is close to 1.2 over a GAI of the wheat crop at the flowering stage around 2.7 (Table 2). The variation in NDVI due to the ear layer is around $\Delta NDVI \approx 0.04$.

For maize crops, the highly scattering tassels in the red and NIR decrease the NDVI values by $\Delta NDVI \approx -0.03$. These results are consistent with those reported by Gitelson (2003).

For the sunflower, the impact is slightly negative ($\Delta NDVI \approx -0.02$) for $\theta_s = 30^\circ$ which is explained mainly by the higher scattering properties of the sunflower heads (Table 2). Conversely, the impact is positive ($\Delta NDVI \approx 0.01$) for $\theta_s = 60^\circ$: under this geometry where the sun is parallel to the rows, the heads cast shadows on the row, inducing a larger decrease of the BRF in the red while NIR BRF remains about the same because of the multiple scattering in the canopy. As expected, for medium solar zenith angles ($\theta_s = 45^\circ$) the impact of the heads is intermediate between the two previous situations with $\Delta NDVI \approx 0$.

Our experimental results also show that the NDVI changes induced by the RO layer can be translated into a change in GAI estimates that can reach up to 25% (Table 4). It can be either positive as in the case of wheat crops and for the sunflower for the smaller solar zenith angle, or negative as in the case of the maize crop.

## 4. Discussion and conclusions

### 4.1. BRF measured by UAVs

We proposed a method to sample the BRDF from UAV multi-angular measurements that appears very efficient as compared to the use of goniometers in the field (Sandmeier and Itten, 1999): it offers the advantage to avoid disturbing the crop surface while using a single footprint where the multiangular observations are concentrated (Roosjen et al., 2016).

Although UAV provides a very promising way to sample the canopy reflectance as demonstrated in this study, uncertainties could be raised in several aspects. We designed carefully the flight plan by taking into account the micro plot size, camera FOV, variation of viewing angles and flight duration. We thus achieved a very good directional sampling of each micro plot. However, around the hotspot direction where very strong variation of canopy reflectance is expected, the sampling density was probably too loose to get a very accurate description of this BRDF feature. Further, the necessary spatial averaging over the microplot induces also a degradation of the directional resolution of the measurements which was around 7°.

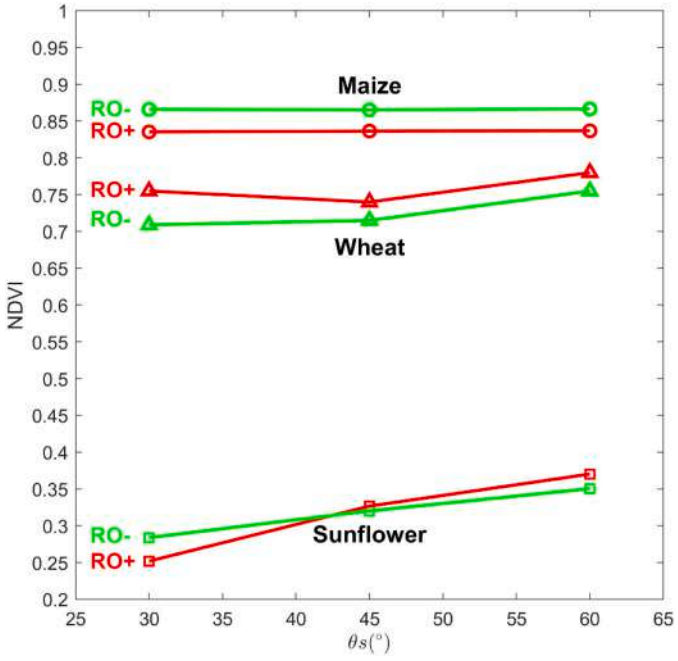


**Fig. 11.** Variation of NDVI values as observed near nadir (average of BRF for $-10\ ^{\circ} < \theta_v < 10^{\circ}$) for maize, sunflower, and wheat with $\theta_s = [30^{\circ}, 45^{\circ}, 60^{\circ}]$. The canopy NDVI values measured with (RO+) and without (RO-) RO are displayed.

**Table 4**
Impact of the RO on GAI estimates. The measured NDVI values for the canopy with (RO+) and without (RO-) RO are displayed along with the corresponding GAI. The difference is then computed in absolute (ΔGAI) or relative value (ΔGAI %). All GAI values are derived from NDVI using the empirical relationship proposed by Verger et al. (2011).

| Species | $\theta_s$ | RO- | | RO+ | | ΔGAI | ΔGAI % |
|---|---|---|---|---|---|---|---|
| | | NDVI | GAI | NDVI | GAI | | |
| Maize | 30° | 0.86 | 4.6 | 0.83 | 3.9 | −0.7 | −15 |
| | 45° | 0.86 | 4.6 | 0.83 | 3.9 | −0.7 | −15 |
| | 60° | 0.87 | 4.8 | 0.83 | 3.9 | −1.0 | −19 |
| Wheat | 30° | 0.70 | 2.2 | 0.76 | 2.7 | 0.5 | 23 |
| | 45° | 0.71 | 2.3 | 0.74 | 2.6 | 0.3 | 13 |
| | 60° | 0.76 | 2.7 | 0.78 | 3.1 | 0.3 | 15 |
| Sunflower | 30° | 0.28 | 0.4 | 0.26 | 0.3 | −0.1 | −25 |
| | 45° | 0.32 | 0.5 | 0.32 | 0.5 | 0.0 | 0 |
| | 60° | 0.36 | 0.6 | 0.37 | 0.6 | 0.0 | 0 |

Our radiometric calibration based on nadir measurements of the reference panel assumes that the irradiance did not change during the flight. This was preferred as compared to using more frequent observations of the panel under the several view directions sampled un order to reduce the uncertainties attached to the BRDF characterization of the panel as well as the illumination geometry. However, the clear sky conditions and the small time interval necessary to complete the flight (7–10 min) ensured that the illumination conditions were about constant during image acquisition. The method also assumes that the camera responds linearly with the radiance and that the black current is neglectable (Smith and Milton, 1999; Wang and Myint, 2015). Although this was verified for few AIRPHEN cameras, using multiple calibration panels in the field as proposed by Pozo et al. (2014) and Smith and Milton (1999) could allow to confirm this important assumption.

### 4.2. Impact of RO on canopy reflectance and NDVI

UAV measurements and 3D model simulations show that the RO have a small effect on the absolute reflectance values, with magnitudes of ±0.02 in the red and ± 0.04 in the NIR band (Fig. 8 and Fig. 9). However, expressed in relative values the differences can reach up to 85% in the red and 34% in the NIR. The impact of RO on canopy reflectance vary with crop, spectral bands and show directional effects. This may translate into substantial changes in vegetation index values: for view directions close to nadir, the wheat ears layer increases the NDVI by up to 0.06 (8.57%), while the maize tassels decrease canopy NDVI by up to 0.04 (4.60%) (Table 4). The sunflower heads impact differently NDVI depending on sun position due to the complex structure and optical properties of the heads, including difference between the two sides and the presence of yellow petals.

These results were derived from measurements acquired at a single date during the crop reproductive stage. However, the impact of RO on reflectance may vary greatly depending on the reproductive stages. For instance, the wheat senescence occurs from the bottom to the top of the canopy and the timing of the disappearance of the chlorophyll pigments in ears will affect the spectral response of the crops (Weiss et al., 2001). Furthermore, the presence of awns, the ear shape or its inclination also vary substantially with the genotype and time, with impact on the spectral and directional behavior on the canopy (Gutierrez et al., 2015). Conversely, for maize, the structure of the tassels is supposed to vary in a lesser extent as compared to wheat, while the yellowing will still have an impact on the spectral variation of the reflectance (Martin et al., 2007). The effect of RO on sunflower reflectance should also be variable depending on the phenological stage as they have the biggest reproductive organs, with contrasted reflectance between each side of the head associated to a complex behavior regarding their orientation due to the heliotropism. Therefore, this study represents a first step to highlight the influence of RO on canopy reflectance but more investigations are required, especially regarding the temporal variations of the spectral properties, the orientation of the organs, genotypic variations and changes in the crop environmental conditions.

### 4.3. Consequences on GAI estimates and applications

The presence of the RO may also impact estimates of GAI. In this study, we used NDVI as a proxy of GAI. Two cases can be considered: (1) if the organs are green and photosynthetically active as in the case of the wheat ears or the sunflower heads, they should be included in the GAI computation since they will contribute to light interception and photosynthesis. However, because the architecture of the reproductive layer at the top of the canopy is different from that of the bottom layer, artifacts may be introduced in the retrieval of GAI if the same architecture is assumed for the two layers. This explains why Weiss et al. (2001) introduced explicitly an ear layer in their dynamic model of wheat canopy architecture. (2) if the RO are not green as for the maize tassels, they will partly absorb and scatter the incoming light without contributing to the GAI. This explains the experimental results from Gitelson et al. (2014) over maize crops who showed that the relationship between the fraction of intercepted radiation and NDVI during the vegetative stage was different from that during the reproductive stage. In both cases, the dynamics of canopy refelectance and NDVI will be altered when the RO are appearing during the flowering stage, leading to possible artifacts on GAI estimation. These artifacts introduced by the presence of the RO layer will depend on the specific structural and optical properties features of each genotype. The perturbations in the dynamics due to the apparition of the RO layer offers the potentials to be exploited to date this important growth stage.

## Declaration of Competing Interest

The authors declare that they have no known competing financial interests or personal relationships that could have appeared to influence the work reported in this paper.

**Acknowledgments**

This study was supported by "Programme d'investissement d'Avenir" PHENOME (ANR-11-INBS-0012). It was carried within the CAPTE-Mixed unit.

**Appendix A**

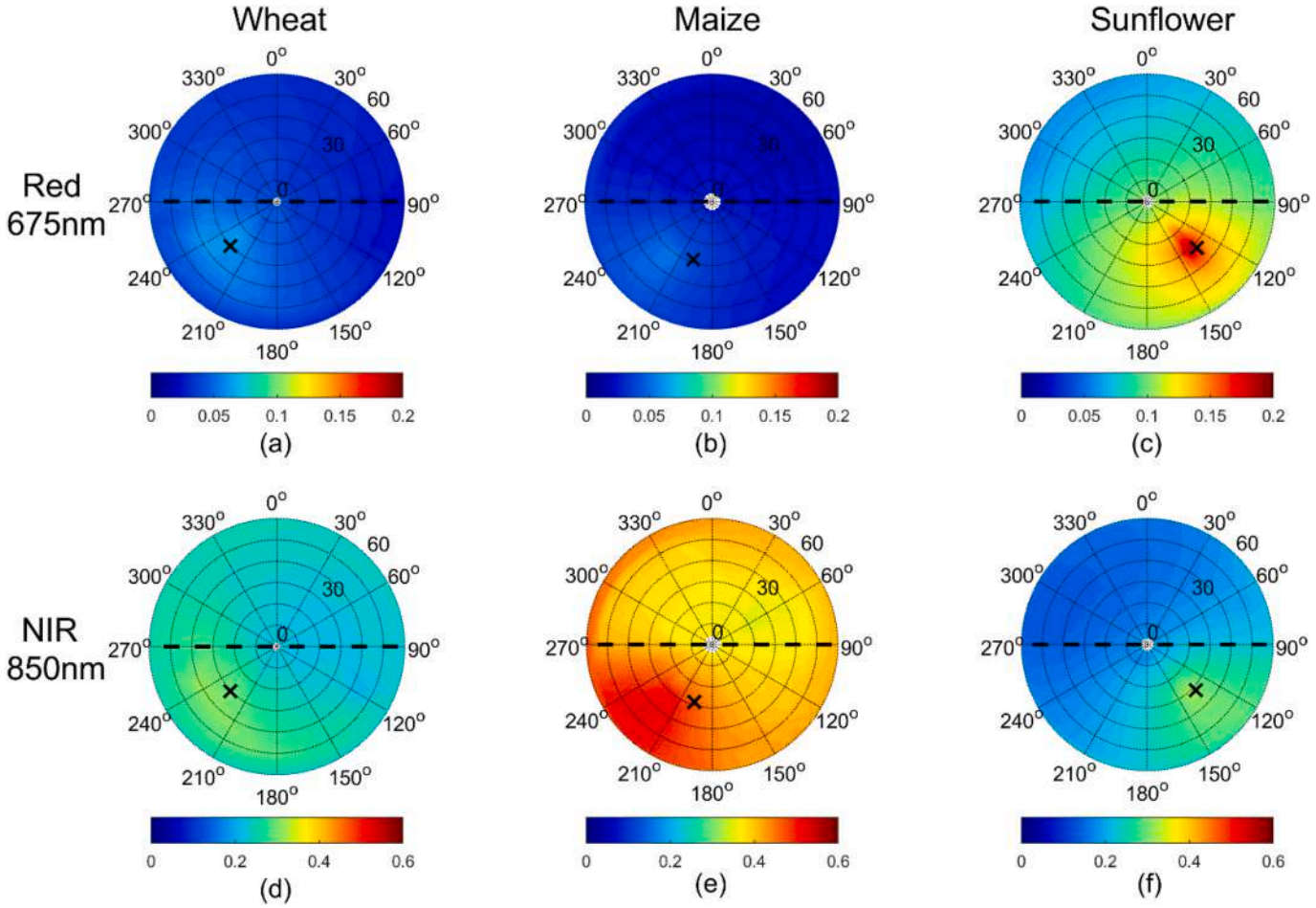


**Fig. A1.** Polar representation of the measured BRF distribution of the three experiments without the RO (RO-) for 675 nm and 850 nm bands. The sun is displayed as a black cross marker and was at $\theta_s$= 30°. The row orientation (east-west) is represented by the dashed black line. Values represent interpolations from raw measured BRF.

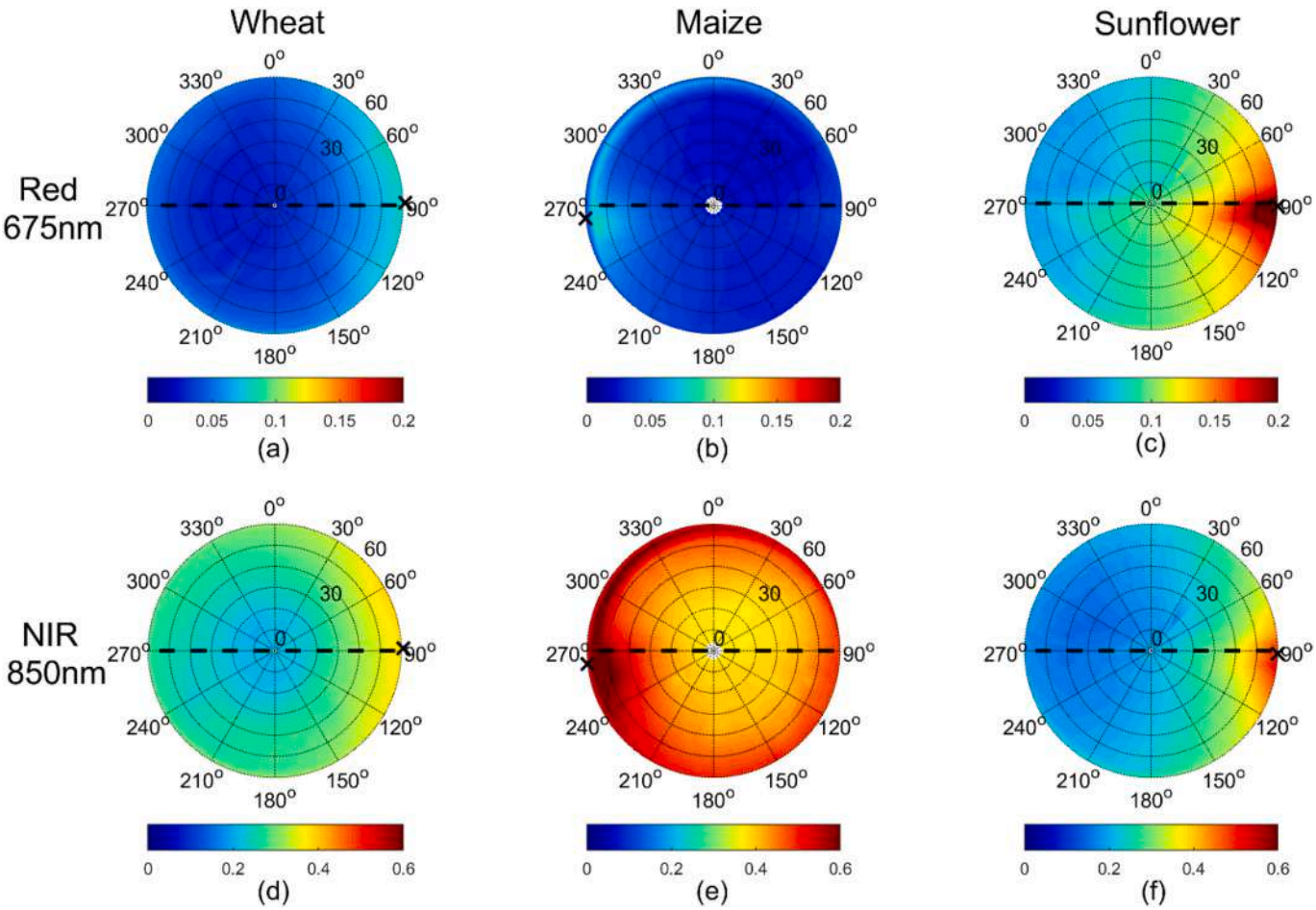


**Fig. A2.** Polar representation of the measured BRF distribution of the three experiments without the RO (RO-) for 675 nm and 850 nm bands. The sun is displayed as a black cross marker and was at $\theta_s$= 60°. The row orientation (east-west) is represented by the dashed black line. Values represent interpolations from raw measured BRF.

## Appendix B

**Table B1**
Measured reflectance of wheat ears, maize tassels, and sunflower petals, front-side and back-side from AIRPHEN camera on 450 nm, 530 nm, and 730 nm. The reflectance of sunflower frontside flower and backside flower does not include yellow petals.

| | 450 nm | 530 nm | 730 nm |
|---|---|---|---|
| Wheat | 0.04 | 0.25 | 0.35 |
| Maize | 0.13 | 0.2 | 0.45 |
| Sunflower front-side | 0.021 | 0.10 | 0.21 |
| Sunflower back-side | 0.06 | 0.17 | 0.38 |
| Sunflower yellow pedal | 0.024 | 0.27 | 0.35 |

## References


Burkart, A., Cogliati, S., Schickling, A., Rascher, U., 2014. A novel UAV-based ultra-light weight spectrometer for field spectroscopy. IEEE Sensors J. 14, 62–67. https://doi.org/10.1109/JSEN.2013.2279720.

Burkart, A., Aasen, H., Alonso, L., Menz, G., Bareth, G., Rascher, U., 2015. Angular dependency of Hyperspectral measurements over wheat characterized by a novel UAV based goniometer. Remote Sens. 7, 725–746. https://doi.org/10.3390/rs70100725.

Casa, R., Jones, H., 2005. LAI retrieval from multiangular image classification and inversion of a ray tracing model. Remote Sens. Environ. 98, 414–428. https://doi.org/10.1016/j.rse.2005.08.005.

Comar, A., Burger, P., de Solan, B., Baret, F., Daumard, F., Hanocq, J.-F., 2012. A semi-automatic system for high throughput phenotyping wheat cultivars in-field conditions: description and first results. Funct. Plant Biol. 39, 914. https://doi.org/10.1071/FP12065.

Cossani, C.M., Reynolds, M.P., 2012. Physiological traits for improving heat tolerance in wheat. Plant Physiol. 160, 1710–1718. https://doi.org/10.1104/pp.112.207753.

Deering, D., Leone, P., 1986. A sphere-scanning radiometer for rapid directional measurements of sky and ground radiance. Remote Sens. Environ. 19, 1–24. https://doi.org/10.1016/0034-4257(86)90038-6.

Disney, M., Lewis, P., Saich, P., 2006. 3D modelling of forest canopy structure for remote sensing simulations in the optical and microwave domains. Remote Sens. Environ. 100, 114–132. https://doi.org/10.1016/j.rse.2005.10.003.

Duthoit, S., Demarez, V., Gastellu-Etchegorry, J.-P., Martin, E., Roujean, J.-L., 2008. Assessing the effects of the clumping phenomenon on BRDF of a maize crop based on 3D numerical scenes using DART model. Agric. For. Meteorol. 148, 1341–1352. https://doi.org/10.1016/j.agrformet.2008.03.011.

España, M.L., Baret, F., Aries, F., Chelle, M., Andrieu, B., Prévot, L., 1999. Modeling maize canopy 3D architecture application to reflectance simulation. Ecol. Model. 122, 25–43.

Génard, M., Baret, F., Simon, D., 2000. A 3D peach canopy model used to evaluate the effect of tree architecture and density on photosynthesis at a range of scales. Ecol. Model. 128, 197–209.
Gitelson, A.A., 2003. Novel technique for remote estimation of CO $_2$ flux in maize. Geophys. Res. Lett. 30, 1486. https://doi.org/10.1029/2002GL016543.
Gitelson, A.A., Peng, Y., Arkebauer, T.J., Schepers, J., 2014. Relationships between gross primary production, green LAI, and canopy chlorophyll content in maize: implications for remote sensing of primary production. Remote Sens. Environ. 144, 65–72. https://doi.org/10.1016/j.rse.2014.01.004.
Goel, N.S., Grier, T., 1987. Estimation of canopy parameters of row planted vegetation canopies using reflectance data for only four view directions. Remote Sens. Environ. 21, 37–51. https://doi.org/10.1016/0034-4257(87)90005-8.
Grenzdörffer, G.J., Niemeyer, F., 2012. UAV based BRDF-measurements of agricultural surfaces with pfifffikus. Int. Arch. Photogramm. Remote. Sens. Spat. Inf. Sci. XXXVIII-1 (C22), 229–234. https://doi.org/10.5194/isprsarchives-XXXVIII-1-C22-229-2011.
Gutierrez, M., Reynolds, M.P., Klatt, A.R., 2015. Effect of leaf and spike morphological traits on the relationship between spectral reflectance indices and yield in wheat. Int. J. Remote Sens. 36, 701–718. https://doi.org/10.1080/01431161.2014.999878.
Hakala, T., Honkavaara, E., Saari, H., Mäkynen, J., Kaivosoja, J., Pesonen, L., Pölönen, I., 2013. Spectral imaging from UAVS under varying illumination conditions. Int. Arch. Photogramm. Remote. Sens. Spat. Inf. Sci. XL-1/W2, 189–194. https://doi.org/10.5194/isprsarchives-XL-1-W2-189-2013.
Holben, B.N., Eck, T.F., Slutsker, I., Tanré, D., Buis, J.P., Setzer, A., Vermote, E., Reagan, J.A., Kaufman, Y.J., Nakajima, T., Lavenu, F., Jankowiak, I., Smirnov, A., 1998. AERONET—A federated instrument network and data archive for aerosol characterization. Remote Sens. Environ. 66, 1–16. https://doi.org/10.1016/S0034-4257(98)00031-5.
Jacob, F., Olioso, A., Weiss, M., Baret, F., Hautecoeur, O., 2002. Mapping short-wave albedo of agricultural surfaces using airborne PolDER data. Remote Sens. Environ. 80, 36–46. https://doi.org/10.1016/S0034-4257(01)00265-6.
Jacob, W., 2014. Mitsuba Documentation Version 0.5.0 [WWW Document]. URL. https://www.mitsuba-renderer.org/.
Jiang, J., Weiss, M., Liu, S., Rochdi, N., Baret, F., 2020. Speeding up 3D radiative transfer simulations: a physically based metamodel of canopy reflectance dependency on wavelength, leaf biochemical composition and soil reflectance. Remote Sens. Environ. 237, 111614. https://doi.org/10.1016/j.rse.2019.111614.
Li, H., Zhao, C., Yang, G., Feng, H., 2015. Variations in crop variables within wheat canopies and responses of canopy spectral characteristics and derived vegetation indices to different vertical leaf layers and spikes. Remote Sens. Environ. 169, 358–374. https://doi.org/10.1016/j.rse.2015.08.021.
Lopez-Lozano, R., Baret, F., García de Cortázar-Atauri, I., Tisseyer, B., Lebon, E., 2009. Reflectance modeling of vineyards under water stress based on the coupling between 3D architecture and water balance model. In: Remote Sensing for Agriculture, Ecosystems, and Hydrology XI. Proceedings of SPIE. Berlin (Germany). https://doi.org/10.1117/12.830057.
LuxCoreRender, 2018. LuxCoreRender Wiki [WWW Document]. URL. https://wiki.luxcorerender.org/LuxCoreRender_Wiki.
Martin, K.L., Girma, K., Freeman, K.W., Teal, R.K., Stone, M.L., Raun, W.R., 2007. Expression of variability in corn as influenced by growth stage using optical sensor measurements. Agron. J. 99, 384–389. https://doi.org/10.2134/agronj2005.0268.
McBratney, A., Whelan, B., Ancev, T., Mcbratney, A., Bouma, J., 2005. Future Directions of Precision Agriculturew, p. 17.
Nicodemus, F.E., Richmond, J.C., Hsia, J.J., Ginsberg, I.W., Limperis, T., 1977. Geometrical Considerations and Nomenclature for Reflectance (no. NBS MONO 160). National Bureau of Standards, Gaithersburg, MD. https://doi.org/10.6028/NBS.MONO.160.
POV-team, 2013. Introduction to POV-Ray for POV-Ray version 3.7 [WWW Document]. URL. http://www.povray.org.
Pozo, S.D., Rodríguez-Gonzálvez, P., Hernández-López, D., Felipe-García, B., 2014. Vicarious Radiometric Calibration of a Multispectral Camera on Board an Unmanned Aerial System, p. 20.
Qin, W., Goel, N.S., 1995. An evaluation of hotspot models for vegetation canopies. Remote Sens. Rev. 13, 121–159. https://doi.org/10.1080/02757259509532299.
Rabatel, G., Labbé, S., 2015. A fully automatized processing chain for high-resolution multispectral image acquisition of crop parcels by UAV. In: Stafford, J.V. (Ed.), Precision Agriculture '15. Wageningen Academic Publishers, The Netherlands, pp. 135–142. https://doi.org/10.3920/978-90-8686-814-8_16.
Ranson, K.J., Daughtry, C.S.T., Biehl, L.L., Bauer, M.E., 1985. Sun-view angle effects on reflectance factors of corn canopies. Remote Sens. Environ. 18, 147–161. https://doi.org/10.1016/0034-4257(85)90045-8.
Roosjen, P., Suomalainen, J., Bartholomeus, H., Clevers, J., 2016. Hyperspectral reflectance anisotropy measurements using a Pushbroom spectrometer on an unmanned aerial vehicle—results for barley, winter wheat, and potato. Remote Sens. 8, 909. https://doi.org/10.3390/rs8110909.
Roujean, J.-L., Leroy, M., Deschamps, P.-Y., 1992. A Bidirectional Reflectance Model of the Earth's Surface for the Correction of Remote Sensing Data, 97, pp. 20455–20468.
Rouse Jr., J.W., Haas, R.H., Schell, J.A., Deering, D.W., 1973. MOMonitoring vegetation systems in the Great Plains with ERTS. Presented at the third earth Resour. Technol. Satell. Symp 309–317. Doi:citeulike-articleid:12009708.
Sandmeier, S.R., Itten, K.I., 1999. A field goniometer system (FIGOS) for acquisition of hyperspectral BRDF data. IEEE Trans. Geosci. Remote Sens. 37, 978–986. https://doi.org/10.1109/36.752216.
Schaepman-Strub, G., Schaepman, M.E., Painter, T.H., Dangel, S., Martonchik, J.V., 2006. Reflectance quantities in optical remote sensing—definitions and case studies. Remote Sens. Environ. 103, 27–42. https://doi.org/10.1016/j.rse.2006.03.002.
Smith, G.M., Milton, E.J., 1999. The use of the empirical line method to calibrate remotely sensed data to reflectance. Int. J. Remote Sens. 20, 2653–2662. https://doi.org/10.1080/014311699211994.
Suits, G.H., 1983. Extension of a uniform canopy reflectance model to include row effects. Remote Sens. Environ. 13, 113–129. https://doi.org/10.1016/0034-4257(83)90017-2.
Verger, A., Baret, F., Camacho, F., 2011. Optimal modalities for radiative transfer-neural network estimation of canopy biophysical characteristics: evaluation over an agricultural area with CHRIS/PROBA observations. Remote Sens. Environ. 115, 415–426. https://doi.org/10.1016/j.rse.2010.09.012.
Verger, A., Vigneau, N., Chéron, C., Gilliot, J.-M., Comar, A., Baret, F., 2014. Green area index from an unmanned aerial system over wheat and rapeseed crops. Remote Sens. Environ. 152, 654–664. https://doi.org/10.1016/j.rse.2014.06.006.
Vermote, E.F., Tanre, D., Deuzé, J.L., Herman, M., Morcrette, J.-J., 1997. Second simulation of the satellite signal in the solar Spectrum, 6S: an overview. IEEE Trans. Geosci. Remote Sens. 35, 675–686.
Viña, A., Gitelson, A.A., Rundquist, D.C., Keydan, G., Leavitt, B., Schepers, J., 2004. Monitoring maize (*Zea mays* L.) phenology with remote sensing. Agron. J. 96, 1139–1147. https://doi.org/10.2134/agronj2004.1139.
Wang, C., Myint, S.W., 2015. A simplified empirical line method of radiometric calibration for small unmanned aircraft systems-based remote sensing. IEEE J. Sel. Top. Appl. Earth Observations Remote Sensing 8, 1876–1885. https://doi.org/10.1109/JSTARS.2015.2422716.
Wanjura, D.F., Hatfield, J.L., 1988. Vegetative and optical characteristics of four-row crop canopies. Int. J. Remote Sens. 9, 249–258. https://doi.org/10.1080/01431168808954849.
Weiss, M., Troufleau, D., Baret, F., Chauki, H., Prévot, L., Olioso, A., Bruguier, N., Brisson, N., 2001. Coupling canopy functioning and radiative transfer models for remote sensing data assimilation. Agric. For. Meteorol. 108, 113–128. https://doi.org/10.1016/S0168-1923(01)00234-9.
Widlowski, J.-L., Robustelli, M., Disney, M., Gastellu-Etchegorry, J.-P., Lavergne, T., Lewis, P., North, P.R.J., Pinty, B., Thompson, R., Verstraete, M.M., 2008. The RAMI on-line model checker (ROMC): a web-based benchmarking facility for canopy reflectance models. Remote Sens. Environ. 112, 1144–1150. https://doi.org/10.1016/j.rse.2007.07.016.
Zhao, F., Gu, X., Verhoef, W., Wang, Q., Yu, T., Liu, Q., Huang, H., Qin, W., Chen, L., Zhao, H., 2010. A spectral directional reflectance model of row crops. Remote Sens. Environ. 114, 265–285. https://doi.org/10.1016/j.rse.2009.09.018.